THE ASTROPHYSICAL JOURNAL, 971:2 (8pp), 2024 August 10 https://doi.org/10.3847/1538-4357/ad6150

The Plasma Pressure Contribution from Low-energy (0.05–2 keV) Energetic Neutral Atoms in the Heliosheath

André Galli[1], Peter Wurz[1], Nathan A. Schwadron[2], Eberhard Möbius[2], Stephen A. Fuselier[3,4], Justyna M. Sokół[3], Paweł Swaczyna[5], Maciej Bzowski[5], and David J. McComas[6]

[1] Space Science and Planetology, Physics Institute, University of Bern, Bern, Switzerland; andre.galli@unibe.ch
[2] University of New Hampshire, Durham, USA
[3] Southwest Research Institute, San Antonio, USA
[4] University of Texas at San Antonio, San Antonio, USA
[5] Space Research Centre PAS (CBK PAN), Warsaw, Poland
[6] Department of Astrophysical Sciences, Princeton University, Princeton, USA
Received 2024 May 22; revised 2024 July 4; accepted 2024 July 8; published 2024 August 1

Abstract

Energetic neutral atoms (ENAs) from the heliosphere are a unique means to remotely image the boundary regions of our heliosphere. The Interstellar Boundary Explorer (IBEX) has been very successful in measuring these ENAs since 2008 at energies from tens of eV to 6 keV. The main question raised by one solar cycle of IBEX-Lo observations at 0.05–2 keV is the strong and ubiquitous underestimation of several model predictions compared with actually measured ENA intensities at energies between 100 and 500 eV. This study converts the observed ENA intensities into plasma pressures for different sky directions and considers the implications for our understanding of the heliosheath and the source of the observed ENAs.

Unified Astronomy Thesaurus concepts: Heliosphere (711); Heliosheath (710); Space plasmas (1544)

1. Introduction

The Interstellar Boundary Explorer (IBEX) is a small explorer mission of NASA, placed in a high-altitude Earth orbit (McComas et al. 2009). IBEX carries two scientific instruments: the energetic neutral atom (ENA) imagers IBEX-Hi (Funsten et al. 2009b) and IBEX-Lo (Fuselier et al. 2009). For this study, we concentrate on IBEX-Lo data at energies from roughly 50 eV to 2 keV.

An ENA is formed when a fast ion (in this paper a proton) exchanges its charge with an ambient neutral atom (in this paper usually neutral hydrogen). The charge-exchange process includes a nearly negligible energy loss, so the ENA then leaves its place of origin with almost the same momentum as the parent ion on a ballistic trajectory and can reach IBEX. The detected ENA intensity j_{ENA} is the line-of-sight integral from IBEX to infinity over the radial component of the proton flux $j_p(r)$ multiplied by the neutral hydrogen density $n_{\mathrm{H}}(r)$, the charge-exchange cross section $\sigma_{p,H}$, and reduced by the survival probability from the source region $s(r)$:

$$j_{\mathrm{ENA}} = \int_{\mathrm{inst}}^{\infty} dr\, j_p(r)\, n_{\mathrm{H}}(r)\, \sigma_{p,H}\, s(r). \tag{1}$$

Measuring heliospheric ENAs with the IBEX instruments thus enables us to obtain a 2D sky map of the proton fluxes outside the termination shock.

The proton populations giving rise to the ENAs observed with IBEX so far were usually (e.g., Fuselier et al. 2021; Galli et al. 2023) assumed to be either pickup ions (PUIs) from the supersonic solar wind or the heliosheath, neutralized in the heliosheath and resulting in the globally distributed ENA flux (Schwadron et al. 2011, 2014), or neutralized solar wind protons passing through the heliopause that are then ionized and neutralized again outside the heliopause in the Very Local Interstellar Medium (VLISM), resulting in the IBEX Ribbon ENAs at solar wind energies (see, e.g., McComas et al. 2020). At energies below 25 eV, also interstellar neutral hydrogen was detected with the IBEX-Lo instrument (Galli et al. 2019; Rahmanifard et al. 2019).

At energies below solar wind energies, there is one major observational challenge to this simple concept of ENA sources: there is a discrepancy of 1 to 2 orders of magnitude between the measured ENA intensities and the much lower intensities predicted by several heliosphere models (Fuselier et al. 2021; Galli et al. 2023). While this is a subject of ongoing model work (see Section 3), we will constrain ourselves here to assessing the implications of this discrepancy on the plasma pressure balance between the heliosphere and the interstellar medium. Linsky & Moebius (2023) recently found that the heliosphere and VLISM can be close to total pressure balance for ion energies >0.5 keV, based on IBEX-Hi, Voyager, Cassini INCA, and other data for the helionose region (where in situ data from Voyager are available). This paper extends this question of plasma pressure balance to the lower energies covered with IBEX-Lo and for regions outside the nose.

2. IBEX-Lo Observations

This work relies on the IBEX-Lo data release 17[7] covering one solar cycle from 2009 to 2019, published by Galli et al. (2022). This data release includes full-sky maps of ENA intensities measured with IBEX-Lo and ENA energy spectra for a selection of sky directions (see Figure 1). For the discussion of plasma pressures in the heliosheath we use the 11 yr averaged ENA spectra transformed to the solar inertial reference frame and corrected for ionization losses from the assumed place of ENA origin to IBEX at 1 au (Tables 4 and 6 in Galli et al. 2022). These ENA energy spectra should thus

[7] https://ibex.princeton.edu/DataRelease17

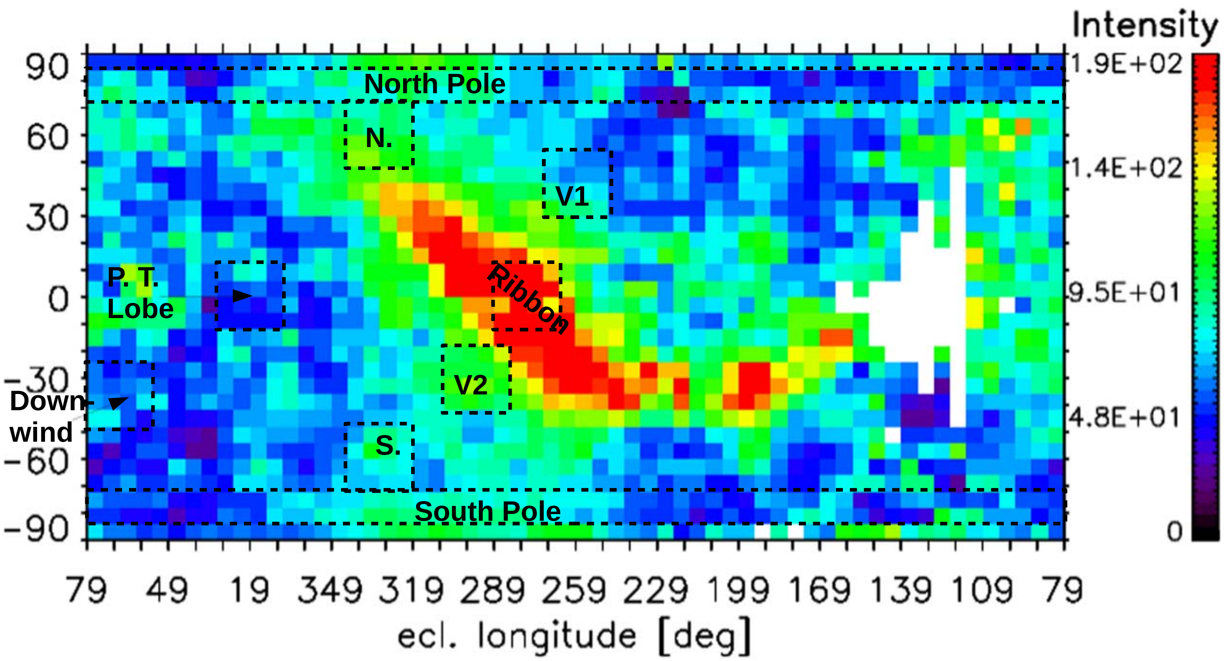

Figure 1. The sky regions defined by Galli et al. (2022), plotted on an ENA intensity map of IBEX-Lo energy bin centered at 0.9 keV averaged over all 11 yr, including corrections for Compton–Getting and ENA survival probability. V1 and V2 denote Voyager 1 and Voyager 2 directions. Figure taken from Galli et al. (2022).

be representative of the protons in the solar inertial frame at the place of ENA generation assuming the ENAs are generated in the heliosheath at an average distance of 100 au (Bzowski 2008).

To derive integrated ENA intensities and hence plasma pressures over an energy range, we added the differential intensities obtained in separate energy bins as an approximate integration. A 10% overestimation of the ENA intensities in the four lowest-energy bins may have been introduced by not subtracting the sputtering contribution from higher- to lower-energy bins for energy bins 1–4 (Fuselier et al. 2012; Galli et al. 2014). Considering that the systematic uncertainties of differential ENA intensities are typically 30% for IBEX-Lo energy bins 5–8 and typically 50% for energy bins 3 and 4 at 50–100 eV (Fuselier et al. 2014; Galli et al. 2014, 2022), we decided to use the published ENA intensities to derive plasma pressures without any reduction factors.

2.1. Background Contributions

At low energies, several background sources are known to exist that were subtracted from the data before analysis (Galli et al. 2022). These include signals from Earth's magnetosphere, the ubiquitous local background identified in the energy bins below 200 eV (Galli et al. 2014), and (for some upstream regions) the inflow of interstellar neutrals (see Galli et al. 2022 for more details). Because the ENA intensities measured with IBEX-Lo below 1 keV exceed model predictions (see the following Section 3), we investigated if an additional global background in IBEX-Lo could explain the ENA data–model discrepancy. This scenario is unlikely for the following reasons:

1. At the overlapping energies (0.7–2 keV), the ENA intensities of the global distributed flux (GDF) and of the ribbon agree between IBEX-Lo and IBEX-Hi.
2. IBEX-Lo clearly measures the ENA ribbon down to at least 200 eV where it becomes broader and starts blending into the GDF. This proves that IBEX-Lo still measures ENAs from the heliospheric boundaries at these energies.
3. If a "dark signal" is postulated to resolve the model–data discrepancy below 700 eV, this would imply that 2/3 of counts in energy bin 6 and 90%–95% of all counts in energy bin 5 would be caused by that "dark signal" whereas it contributes a negligible amount in energy bin 7.
4. As a further consequence of such a "dark signal" mimicking the GDF, the actual ribbon/GDF intensity ratios below 700 eV would increase to ratios ($\geqslant 3$) higher than ever encountered at solar wind energies.
5. The measured raw count rates in energy bin 5 show an obvious dichotomy between ram and antiram directions (see Figure 2 as an example). This is only possible if the source of the signal does not originate in the reference frame of IBEX or the Earth, but in the solar/heliosphere reference frame instead.

Such an unexplained background would thus be just another label for a global heliospheric ENA source moving at 1 au perpendicularly to the Sun–Earth line and not strongly varying over the course of one solar cycle (see Figures 1 and 10 in Galli et al. 2022). The physical process creating these additional low-energy ENAs has to be found in any case.

3. Previous Data–Model Comparisons

In previous studies, Fuselier et al. (2021) compared the measured IBEX-Lo energy spectra of the globally distributed ENA flux with two PUI models (Heerikhuisen et al. 2019; Fuselier et al. 2021), initially assuming that the majority of these ENAs originate from PUIs in the heliosheath. Both PUI models assumed a multicomponent suprathermal ion model with the same solar wind and PUI populations with one model assuming Maxwellian distributions for all PUI populations and the other assuming a power law ($\sim E^{-2.5}$) starting at the outer radius of the

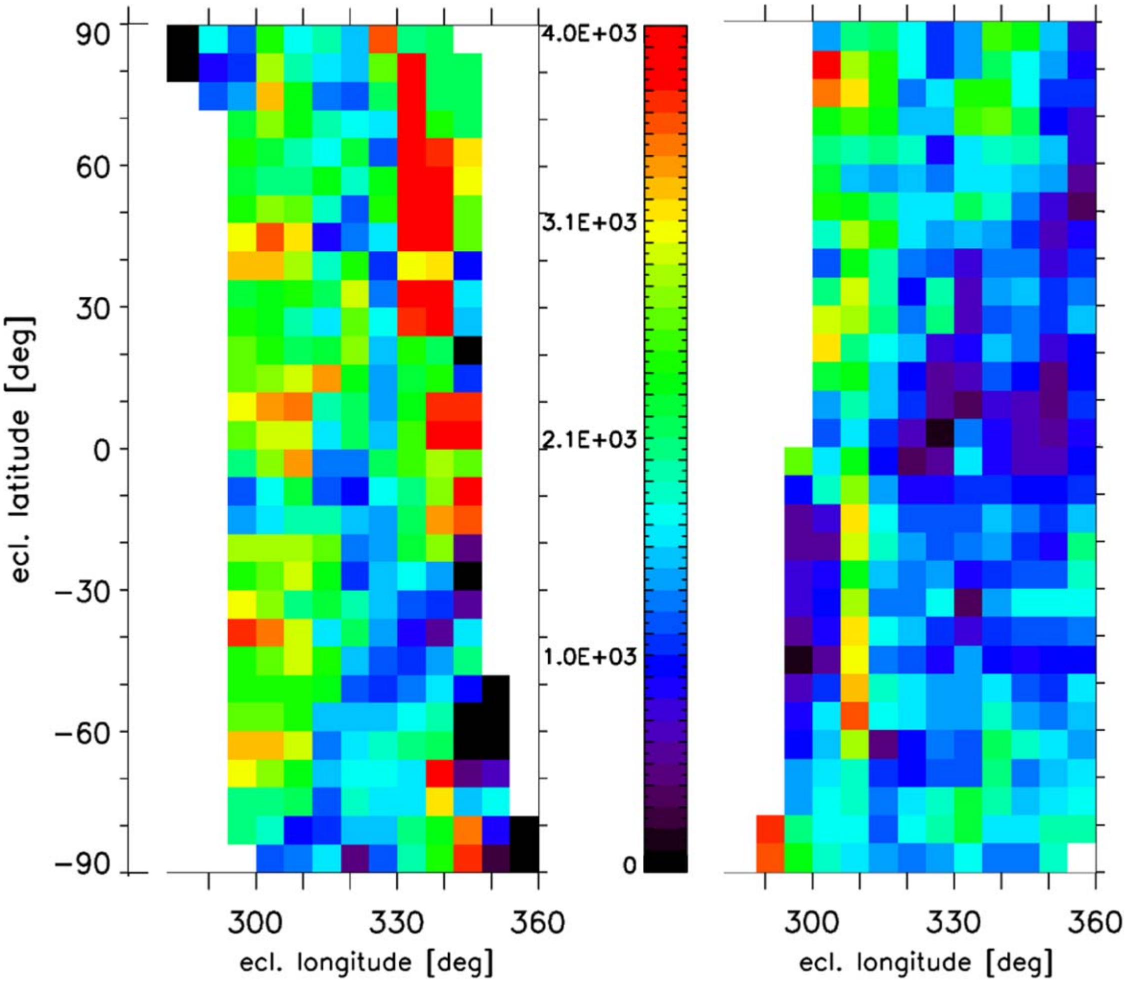

Figure 2. Raw ENA intensities without survival probability or Compton–Getting correction measured in IBEX-Lo energy bin 5 in the season 2009/2010 at ecliptic longitudes 300°–360° and ecliptic latitudes from −90° to +90° in ram directions (left panel) and antiram directions (right panel). The central color scale in units of $\mathrm{cm^{-2}\,sr^{-1}\,s^{-1}\,keV^{-1}}$ applies to both panels.

PUI shell. Fuselier et al. (2021) came to the conclusion that the ENA intensities from inner heliosheath sources included in their models amounted to a maximum of ∼10% of the actually observed ENA intensities for most energies between 50 eV and 1 keV. This is illustrated in the right panel of Figure 3. More recently, Galli et al. (2023) compared the ENA intensity spectra, averaged over an entire solar cycle, with two other heliosphere models (Baliukin et al. 2020; Kornbleuth et al. 2023): the left panel of Figure 3 shows the comparison of measured with the modeled ENA energy spectra averaged over all sky regions, with the discrepancy between modeled and observed ENA intensities colored in blue (Galli et al. 2023). Both studies thus reached the same conclusion that the model predictions underestimate the observed ENA intensities by 1 to 2 orders of magnitude in all sky directions at ENA energies between 100 and 500 eV. Zirnstein et al. (2018a, 2018b) showed that energy diffusion due to a combination of Alfvénic and compressive turbulence in the heliosheath (HS) can reproduce the ENA energy spectrum measured with IBEX-Lo and IBEX-Hi in the direction of the heliotail, but the specific type of turbulence and the potential role of reconnection events for creating the observed ENA intensities still need to be studied (Galli et al. 2023). Either a significant process for ENA generation in the heliosheath is overlooked or there is an additional low-energy ENA source beyond the heliopause.

4. Results

In the following, we convert the observed ENA intensities into plasma pressures depending on the plasma bulk speed and compare the results to previous studies on pressure balance in the heliosheath. The plasma pressure derived from ENAs is important for the overall pressure balance of the heliosheath, but it is not the only contribution to the total pressure. Linsky & Moebius (2023), e.g., differentiated between six types of pressures: magnetic pressure, thermal pressure, ram pressure, cosmic-ray pressure, turbulent pressure, and suprathermal pressure. This latter pressure is synonymous with "plasma pressure" or "PUI pressure," and it is the pressure contribution sampled with IBEX as ENAs.

4.1. Plasma Pressure Derived from IBEX ENA Intensities

Without the aid of any heliospheric model, the ENA intensities observed with IBEX can be transformed into plasma pressure times length of the ENA production region based on three assumptions. The first is that IBEX observes ENAs from those parent ions (with a proton velocity distribution function $f(v_p)$) that were moving radially inward in the heliosheath at the time of charge exchange. The total outward radial pressure of these parent ions, embedded in the solar wind bulk flow moving at a radial speed u_R with respect to the solar inertial

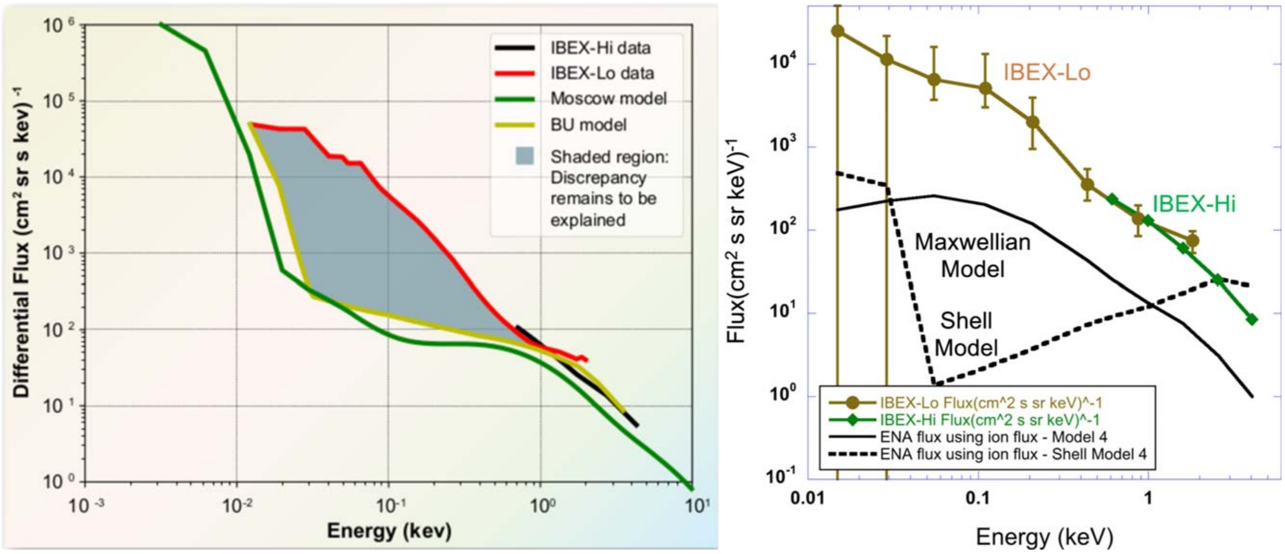

Figure 3. Discrepancy between measured and modeled ENA intensities. Left panel: measured (red and black lines) and modeled (dark and light green lines) ENA intensities, averaged over all sky regions noted in Figure 1 (figure taken from Galli et al. 2023). Right panel: measured (olive and green lines) and modeled (black solid and dashed lines) ENA intensities for Voyager 2 direction (figure taken from Fuselier et al. 2021).

reference frame, includes the internal plasma pressure and the ram plasma pressure (Schwadron et al. 2011):

$$P_p = \frac{4\pi m}{3}\int_{v_{\min}}^{v_{\max}} dv_p\, v_p^4 f(v_p) + 4\pi m u_R^2 \int_{v_{\min}}^{v_{\max}} dv_p\, v_p^2 f(v_p). \tag{2}$$

In the following, we will neglect the ram pressure contribution of the shocked solar wind, which calculates to

$$P_{p,\mathrm{ram}} = \rho\, v_{\mathrm{HS}}^2 \approx 0.03\,\mathrm{pPa} = 0.3\,\mathrm{pdyne\,cm^{-2}}, \tag{3}$$

with a solar wind speed of $v_{\mathrm{HS}} \approx u_R \approx 100\,\mathrm{km\,s^{-1}}$ and an average density of $n_{\mathrm{SW}} = 2 \times 10^3\,\mathrm{m^{-3}}$ in the heliosheath (Richardson et al. 2022). This ram pressure is 1 order of magnitude lower than the typical pressure derived from the first term or the total plasma pressure expected from theory (see Section 4.3). The second assumption is Equation (1), i.e., we assume the distribution function of ENAs, $f_{\mathrm{ENA}}(v_p)$, in the plasma frame is related to the proton velocity distribution function via $f_{\mathrm{ENA}}(v_p) = f_p(v_p) n_{\mathrm{H}}\, \sigma(E) l$ with the integration length l in the heliosheath. Finally, we want to interpret ENA measurements transformed into the solar inertial reference frame, relative to which the local plasma frame is moving with the speed u_R. The ENA velocity is directed radially inward toward the observer in such a way that $v_p^2 = (v_{\mathrm{ENA}} + u_R)^2$ (Schwadron et al. 2011). With these assumptions in place, the plasma pressure times the heliosheath length ($\Delta P \times l$) can be derived from the IBEX ENA energy spectra as the product of a stationary pressure (the internal plasma pressure in the inertial reference frame with $u_R = 0$) times a correction factor c_f (Funsten et al. 2009a; Schwadron et al. 2011; Fuselier et al. 2012):

$$\Delta P \times l = \frac{4\pi\sqrt{2m}}{3 n_{\mathrm{H}}} \frac{j_{\mathrm{ENA}}(E_0)}{\sigma(E_0)} \int_{E_0-\Delta E/2}^{E_0+\Delta E/2} dE \sqrt{E} \left(\frac{E}{E_0}\right)^{-\gamma} c_f \tag{4}$$

$$c_f = \frac{(v_{\mathrm{ENA}} + u_R)^4}{v_{\mathrm{ENA}}^4}. \tag{5}$$

Equation (4) without the correction factor c_f describes the case of a source ion population for the observed ENAs that is spatially isotropic in the solar inertial reference frame (Funsten et al. 2009a; Schwadron et al. 2011), which is equivalent to stating $u_R = 0$.

The energy integral is performed for an IBEX energy bin with the energy bin widths $\Delta E/E \approx 0.7$ known from calibration and with the measured ENA intensity j_{ENA} at the bin center energy E_0. The spectral index γ describes the power law of the ENA energy spectrum (which may vary with time and for different energy bins). The neutral hydrogen density n_{H} in the heliosheath is assumed to be $0.13\,\mathrm{cm^{-3}}$ (Swaczyna et al. 2020).[8]

Equation (4) is similar to the approximation by Galli et al. (2017) where the integration over energy is replaced by the central value times the bin width ΔE and $E = m v_{\mathrm{ENA}}^2/2$ is used:

$$\Delta P \times l \approx \frac{2\pi m^2}{3 n_{\mathrm{H}}} \frac{\Delta E}{E} \frac{j_{\mathrm{ENA}}}{\sigma(E)} \frac{(v_{\mathrm{ENA}} + u_R)^4}{v_{\mathrm{ENA}}}. \tag{6}$$

Equation (4) is also equivalent (save the different integration limits) to the term in Equation (3) of Reisenfeld et al. (2021) if the heliosheath plasma were at rest in the Sun's rest frame, i.e., if $u_R = 0$:

$$\Delta \bar{P} \times l = \frac{4\pi\sqrt{2m}}{3 n_{\mathrm{H}}} \int_{E_i}^{E_{i+1}} dE \frac{\sqrt{E}}{\sigma(E)} j_{\mathrm{ENA}}(E_i) \left(\frac{E}{E_i}\right)^{-\gamma_i}. \tag{7}$$

In this study, we use Equation (4) by default unless otherwise stated; ΔP denotes dynamic pressure and $\Delta \bar{P}$ denotes stationary pressure for $c_f = 1$.

The plasma bulk speed u_R in the heliosheath is not constrained by in situ measurements apart from the Voyager trajectories and therefore depends on model assumptions; u_R is

[8] Increasing n_{H} in the heliosheath toward the heliopause up to about $0.2\,\mathrm{cm^{-3}}$ (Swaczyna et al. 2024) would lead to a roughly 30% decrease of inferred plasma pressures according to Equation (4).

Table 1
Pressure Times Line of Sight for the South and North Energy Spectra (11 yr Averages, Ram Observations) for the Dynamic and Stationary ($u_R = 0$) Cases

E (keV)	$\Delta P \times l$ (pdyne cm^{-2} au)		$\Delta \bar{P} \times l$ (pdyne cm^{-2} au)	
	South	North	South	North
0.02	⩽186	⩽155	⩽4	⩽3
0.04	⩽74	⩽71	⩽3	⩽3
0.09	67	67	7	7
0.18	35	40	6	7
0.39	13	16	4	5
0.81	13	17	5	7
1.73	21	24	11	13

Note. Pressure times line of sight calculated with Equation (4). Relative uncertainties are 50% between 50 and 100 eV and 30% at higher energies; entries below 50 eV are only upper limits.

Table 2
Pressure Times Line of Sight for the South Pole and North Pole Energy Spectra (11 yr Averages, Ram Observations) for the Dynamic ($u_R = 100$ km s^{-1}) and Stationary ($u_R = 0$) Cases

E (keV)	$\Delta P \times l$ (pdyne cm^{-2} au)		$\Delta \bar{P} \times l$ (pdyne cm^{-2} au)	
	South Pole	North Pole	South Pole	North Pole
0.03	⩽403	⩽452	⩽11	⩽13
0.05	⩽127	⩽84	⩽8	⩽5
0.10	61	50	7	6
0.20	39	31	7	6
0.42	8	9	2	3
0.84	7	8	3	3
1.78	13	14	7	7

Note. Pressure times line of sight calculated with Equation (4). Relative uncertainties are 50% between 50 and 100 eV and 30% at higher energies; entries below 50 eV are only upper limits.

expected to vary with heliosheath region and solar cycle between 40 and 200 km s^{-1} (Zirnstein et al. 2021). The solar cycle variability of the solar wind leaves visible imprints on the observed ENA signal at solar wind energies or higher energies in annual ENA maps (McComas et al. 2024). However, these variations become weaker toward lower ENA energies because the traceback time between original solar wind and received ENA increases: a 200 eV ENA from the heliosheath has a traceback time of almost one solar cycle (Galli et al. 2022). Moreover, the ENA energy spectra used in this study have been averaged over an entire solar cycle (Galli et al. 2022), removing any shorter term variability. To cover a plausible range of plasma bulk speeds and to demonstrate their effects on the derived plasma pressure, we will both calculate the stationary pressure (i.e., assuming $u_R = 0$) and the dynamic pressure assuming a universal plasma bulk speed of $u_R = 100$ km s^{-1} as a rough average over all heliosheath regions and one solar cycle for all directions (see Tables 1–5). We will then consider a more nuanced approach with regionally different plasma bulk speeds based on a heliosphere model (see Section 4.2 and Table 6).

Tables 1–3 list the plasma pressures times length for the energy spectra of ENA ram observations in Galli et al. (2022), calculated with Equation (4): the first and second column show the dynamic pressure based on $u_R = 100$ km s^{-1}, the third and forth column list the stationary pressure for which $u_R = 0$ are assumed. The central energies listed in Tables 1–5 differ for

Table 3
Pressure Times Line of Sight for the Voyager 1 and Voyager 2 Energy Spectra (11 yr Averages, Ram Observations) for the Dynamic ($u_R = 100$ km s^{-1}) and Stationary ($u_R = 0$) Cases

E (keV)	$\Delta P \times l$ (pdyne cm^{-2} au)		$\Delta \bar{P} \times l$ (pdyne cm^{-2} au)	
	Voyager 1	Voyager 2	Voyager 1	Voyager 2
0.01	⩽424	⩽176	⩽5	⩽2
0.03	⩽127	⩽62	⩽5	⩽2
0.08	45	52	4	5
0.16	31	34	5	6
0.37	10	14	3	4
0.77	10	15	4	6
1.68	16	22	8	11

Note. Pressure times line of sight calculated with Equation (4). Relative uncertainties are 50% between 50 and 100 eV and 30% at higher energies; entries below 50 eV are only upper limits.

Table 4
Pressure Times Line of Sight for the South and North Energy Spectra (11 yr Averages, Antiram Observations) for the Dynamic ($u_R = 100$ km s^{-1}) and Stationary ($u_R = 0$) Cases

E (keV)	$\Delta P \times l$ (pdyne cm^{-2} au)		$\Delta \bar{P} \times l$ (pdyne cm^{-2} au)	
	South	North	South	North
0.04	⩽503	⩽503	⩽23	⩽23
0.07	180	135	15	11
0.13	89	96	12	13
0.24	67	62	14	13
0.48	16	21	5	7
0.93	14	19	6	8
1.91	22	25	12	14

Note. Pressure times line of sight calculated with Equation (4). Relative uncertainties are 50% between 50 and 100 eV and 30% at higher energies; entries below 50 eV are only upper limits.

Table 5
Pressure Times Line of Sight for the Downwind and Port Lobe Energy Spectra (11 yr Averages, Antiram Observations) for the Dynamic ($u_R = 100$ km s^{-1}) and Stationary ($u_R = 0$) Cases

E (keV)	$\Delta P \times l$ (pdyne cm^{-2} au)		$\Delta \bar{P} \times l$ (pdyne cm^{-2} au)	
	Downwind	Port Lobe	Downwind	Port Lobe
0.05	⩽355	⩽616	⩽20	⩽42
0.09	112	146	11	15
0.15	64	107	10	17
0.27	45	69	10	16
0.52	11	15	4	5
0.99	12	12	5	5
1.99	20	18	11	10

Note. Pressure times line of sight calculated with Equation (4). Relative uncertainties are 50% between 50 and 100 eV and 30% at higher energies; entries below 50 eV are only upper limits.

Table 6
Dynamic Plasma Pressures (in Units of pdyne cm^{-2}) Derived for All Sky Regions with the Stated Interaction Length Scales in the Heliosheath from the Results in Tables 1–5 for Energies above 50 eV

Region Length Scale (au)	South 45	North 80	South Pole 45	North Pole 80	Voyager 1 35	Voyager 2 35	Downwind 200	Port Lobe 200
Pressure, $u_R \equiv 100$ km s^{-1}	3.3	2.1	2.8	1.4	3.2	3.9	1.3	1.8
Pressure, regional u_R	5.9	3.4	5.4	2.5	1.9	2.4	1.6	1.6

different regions because the Compton–Getting transformation to the solar reference frame depends on viewing direction. Usage of the approximation (Equation (6)) tends to result in slightly lower-pressure products (specifically, for all energy bins in the "South" spectrum, the numbers calculated with Equation (6) are 0.85 ± 0.07 times the numbers calculated with Equation (4)). However, these changes are smaller than the uncertainty of the ENA intensities, which is at least 30% (Galli et al. 2022). At ENA energies above 0.3 keV where $v_{\rm ENA}$ is much larger than the plasma bulk flow speed, the energy bins show similar contributions to the total pressure (see Tables 1–3) because of the given ENA spectral slope (Schwadron et al. 2011, 2014). Figure 4 illustrates the pressure times line of sight versus ENA energy for the ram observations of South and North regions listed in Table 1.

For the South region spectrum e.g., the reanalysis presented in Table 1 indicates an integrated pressure times length scale of 149 ± 36 pdyne cm^{-2} au between 0.06 and 2.5 keV compared with 148 ± 30 pdyne cm^{-2} au by Galli et al. (2017) for 0.08–2.3 keV. Note that these error bars neglect the uncertainty of the plasma bulk flow speed.

ENA antiram observations at low energies are affected by less favorable signal-to-noise ratios and backgrounds (see Galli et al. 2022 and references therein). Tables 4 and 5 list the derived pressure products for the four sky regions for which antiram energy spectra were calculated by Galli et al. (2022). Note that the South and North regions in Table 4 denote the same sky regions as those in Table 1, albeit with an energy shift due to the transformation into the solar inertial reference frame. Comparing between ram and antiram observations for, e.g., the South region, we find that $\Delta P \times l = 208$ pdyne cm^{-2} au summed over the five energy bins above 70 eV for antiram observations in contrast to the 149 pdyne cm^{-2} au for ram observations. This difference indicates that the antiram ENA observations around 100 eV are still affected by local background at IBEX to some extent (also see Figure 8 in Galli et al. 2022).

From the Tables 1–5, plasma pressures can be estimated under the assumption of an interaction length scale. The latter is equal to or smaller than the heliosheath thickness provided these ENAs are mostly PUIs from the heliosheath. For the nose direction of the heliosphere (Voyager 1 and Voyager 2 spectra), we know that $l = 35$ au. For North Pole regions $l = 70$–90 au, for South Pole regions $l = 40$–50 au (Reisenfeld et al. 2021). Note that the heliosheath toward the South Pole regions is predicted to be considerably thicker (60–80 au) by some heliosphere models (Pogorelov et al. 2016; Zirnstein et al. 2021; Bera et al. 2023).

For the downwind hemisphere directions, we assume an interaction length = minimum(cooling length, neutralization length) = 200 au for all IBEX-Lo energies (Galli et al. 2017; Reisenfeld et al. 2021). The results are shown in Table 6. All entries from energies above 50 eV in Tables 1–5 were included. For South and North spectra, the ram observations were used; the dynamic pressure derived from antiram observations was higher by a factor of 2 when integrated over a comparable energy interval. Considering the intrinsic uncertainties of the measured ENA intensities at low energies, the relative uncertainty of the plasma pressures in Table 6 is roughly 50% without the uncertainties associated with plasma bulk speed and interaction lengths.

4.2. A More Refined Approach to Plasma Bulk Speed

To obtain more realistic plasma bulk speeds u_R, we investigated different approaches: the analytical model introduced by Schwadron et al. (2011) and Schwadron et al. (2014) calculates the plasma bulk speed downstream of the termination shock by solving the shock jump relation using the upstream Mach number with an adiabatic index $\gamma = 5/3$. For instance, the downstream speed calculates to 144 km s^{-1} for a solar wind speed of 375 km s^{-1} at 1 au, a termination shock distance of 85 au, and a shock jump ratio of roughly 2 (Schwadron et al. 2011). For other sky directions, the u_R results usually range between 150 and 240 km s^{-1} for realistic solar wind speeds at 1 au and termination shock distances between 90 and 120 au. Because the analytical model is one-dimensional, this variation is obtained by varying the initial solar wind speed at 1 au and the termination shock distance. Varying the neutral hydrogen density inside the termination shock between 0.1 and 0.13 cm^{-3} has minor effects on the derived u_R. These values for the radial bulk speed tend to be higher than the line-of-sight-integrated simulation results derived by Zirnstein et al. (2021; see Figure 5). One likely explanation for this difference between model results is that the radial profile of u_R is not constant but rather decreases notably with distance in the heliosheath. We therefore repeated the pressure calculations with the average u_R values simulated by Zirnstein et al. (2021; South: 145 km s^{-1}; North: 140 km s^{-1}; South Pole: 150 km s^{-1}; North Pole: 145 km s^{-1}; Voyager 1 and 2: 65 km s^{-1}; Downwind: 115 km s^{-1}; Port Tail Lobe: 90 km s^{-1}). The resulting plasma pressures are displayed in the bottom row of Table 6.

4.3. Implications for Source of Globally Distributed ENAs below Solar Wind Energy

First, the pressure results in Table 6 confirm that the ram pressure contribution of the shocked solar wind or plasma bulk flow is 1 order of magnitude lower than the plasma pressure from PUIs in the heliosheath implied by the heliospheric ENAs. More surprisingly, the plasma pressures for directions far away from the ecliptic plane ($\geqslant 2.5$ pdyne cm^{-2} for a realistic average plasma bulk speed; see lower row in Table 6) seem notably higher than previous estimates for plasma pressure: Livadiotis et al. (2013) modeled plasma pressures of typically 2 pdyne cm^{-2} = 0.2 pPa for the entire energy range from the globally distributed ENA flux based on measurements with IBEX-Lo and IBEX-Hi. Linsky & Moebius (2023) used

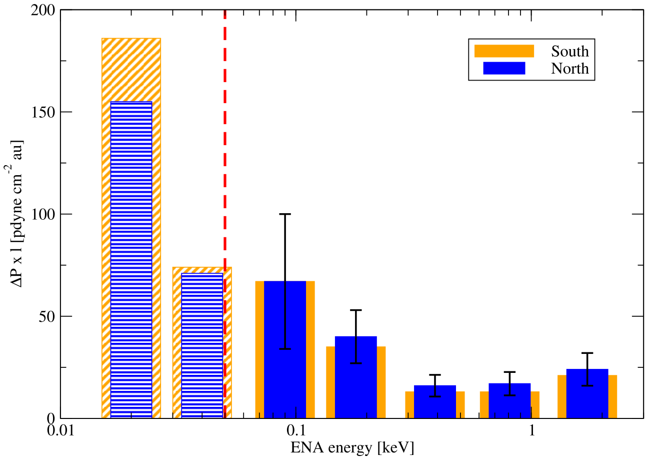

Figure 4. Dynamic pressure times line of sight for the South (orange bars) and North (blue bars) energy spectra (second and third columns in Table 1). For the sake of visibility, the (similar-sized) error bars are only shown for one of the two regions. The values below 50 eV energy (red dashed line) are upper limits of the actual pressure times line of sight.

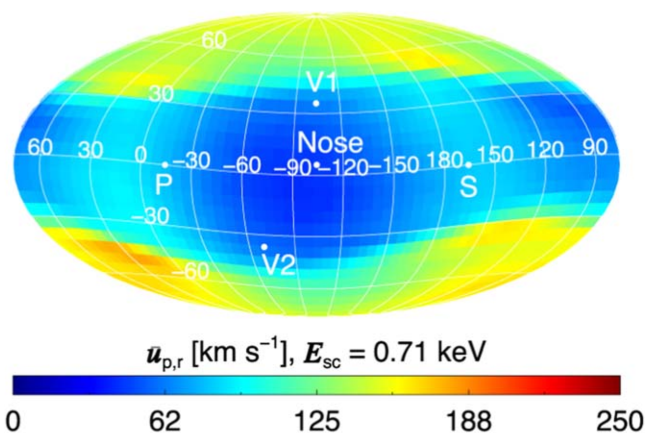

Figure 5. Sky map of the line-of-sight-averaged radial plasma flow speed u_R predicted for an ENA energy of 0.71 keV in the spacecraft reference frame. Figure taken from Zirnstein et al. (2021; their Figure 4, middle top row).

30 pdyn cm^{-2} au for the average and the nose region plasma pressure derived from IBEX-Hi measurements between 0.5 and 4.3 keV (McComas et al. 2014), which (with heliosheath thickness = 35 au toward the nose) implies a plasma pressure of 0.086 pPa. The authors obtained $P = 0.25$ pPa as total pressure for the nose region of the heliosphere without the dynamic pressure as a sum of plasma pressure, magnetic pressure, thermal pressure, ram pressure, cosmic-ray pressure, and turbulent pressure. Above 0.5 keV, the plasma pressure and the GCR pressure dominate the total pressure (Linsky & Moebius 2023). The plasma pressure of the IBEX Ribbon outside the heliopause was also estimated to 2 pdyne cm^{-2} for an assumed radial ribbon thickness of 50 au (McComas et al. 2014).

We conclude that the plasma pressure derived from ENAs of the GDF between 0.05 and 2.5 keV appears to be higher than expected from models for the upwind hemisphere and for polar regions,[9] in particular. There are two caveats about this statement: first, the ENA intensities around or below 100 eV, which dominate the derived dynamical pressure, have a total uncertainty of roughly 50% (Galli et al. 2022; also because of the intense interstellar neutra, ISN, signal at these energies). Second, the derived pressures also depend on assumed length scale, neutral hydrogen density, and plasma bulk speed in the heliosheath (see Equation (4)). Whereas the first two parameters affect the derived pressure linearly, the impact of the plasma bulk speed is nonlinear and would particularly increase the derived pressure if the real $u_R > 100$ km s^{-1}. The two scenarios considered in this study for universal or more accurate regional values of u_R underline the importance of better understanding the plasma flow speeds in the heliosheath in all directions and at varying radial distances. In addition, the discrepancy between plasma pressures inferred from IBEX-Lo and previous studies favoring pressures of roughly 1 pdyne cm^{-2} between 0.05 and 2.5 keV is concentrated to high-latitude regions (most obviously the South and South Pole regions) with their higher plasma bulk speeds. For directions close to the ecliptic (including the two cases in the downwind hemisphere), the inferred plasma pressure accounts to typically 1–2 pdyne cm^{-2} for realistic plasma bulk speeds (see Table 6), which means there is no significant pressure excess in these directions.

Galli et al. (2023) suggested two mutually not exclusive explanations for the discrepancy between observed and predicted ENA intensities: higher PUI fluxes in the heliosheath through turbulence processes, e.g., velocity diffusion of 0.1–5 keV protons in the heliosheath (Zirnstein et al. 2018b), could result in the measured ENA intensities, but the specific physical mechanism has not been identified so far. On the other hand, some ENA sources probably originate in the VLISM, i.e., from outside the heliopause (also see Fuselier et al. 2021), implying that a part of the proton fluxes inferred from the ENAs do not contribute to the plasma pressure inside the heliosheath. Possible extraheliosphere ENA contributions are accelerated ISN hydrogen or secondary ENAs in analogy to the secondary ENAs postulated for the Ribbon ENAs (but more uniformly distributed throughout the VLISM).

These hypotheses will be corroborated or ruled out by the complementary set of observations by the Interstellar Mapping and Acceleration Probe, to be launched in 2025 (McComas et al. 2018). A new complete set of in situ measurements of ions in the heliosheath and their implications on pressure balance will hopefully follow in the farther future thanks to the Interstellar Probe (Brandt et al. 2023; Dialynas et al. 2023).

5. Conclusions

The intensities of the globally distributed ENAs from the heliosphere between 0.05 and 0.5 keV measured with IBEX considerably exceed ENA intensities predicted with several independent heliosphere models. The present study has reassessed this problem by interpreting the observed ENA intensities as plasma pressure in the heliosheath.

The plasma pressure derived from the ENA spectra under the assumption that they are all PUIs inside the heliosheath results in a partial pressure that is hard to reconcile with estimates of total plasma pressure in the heliosheath toward polar regions. Our conjecture, in agreement with previous data–model comparisons (Fuselier et al. 2021; Galli et al. 2023), is that a sizable fraction of the GDF ENAs observed below solar wind energy originate from outside the heliopause and/or that acceleration processes are relevant in the heliosheath that are so far not represented in heliospheric ENA models.

[9] The plasma pressure would still exceed 3 pdyne cm^{-2} toward the South Pole even for a heliosheath thickness of 80 au.

Acknowledgments

We thank all of the outstanding people who have made the IBEX mission such a wonderful success. N.A.S., E.M., S.A.F., J.M.S., and D.J.M. were all funded by the IBEX mission as part of NASA's Explorer Program (80NSSC18K0237). P.S. is supported by a project cofinanced by the Polish National Agency for Academic Exchange within the Polish Returns Programme (BPN/PPO/2022/1/00017), with a research component funded by the National Science Centre, Poland (2023/02/1/ST9/00004). M.B. was supported by a Polish National Science Centre grant 2019/35/B/ST9/01241. This paper benefited from the International Space Science Institute (ISSI) in Bern, through ISSI International Team project No. 541 (Distribution of Interstellar Neutral Hydrogen in the Sun's Neighborhood).

Conflict of Interest

The authors declare that they have no conflict of interest.

References

Baliukin, I. I., Izmodenov, V. V., & Alexashov, D. B. 2020, MNRAS, 499, 441
Bera, R. K., Fraternale, F., Pogorelov, N. V., et al. 2023, ApJ, 954, 147
Brandt, P. C., Provornikova, E., Bale, S. D., et al. 2023, SSRv, 219, 18
Bzowski, M. 2008, A&A, 488, 1057
Dialynas, K., Sterken, V. J., Brandt, P. C., et al. 2023, FrASS, 10, 58
Funsten, H. O., Allegrini, F., Crew, G. B., et al. 2009a, Sci, 326, 964
Funsten, H. O., Allegrini, F., Bochsler, P., et al. 2009b, SSRv, 146, 75
Fuselier, S. A., Allegrini, F., Bzowski, M., et al. 2012, ApJ, 754, 14
Fuselier, S. A., Allegrini, F., Bzowski, M., et al. 2014, ApJ, 784, 89
Fuselier, S. A., Bochsler, P., Chornay, D., et al. 2009, SSRv, 146, 117
Fuselier, S. A., Galli, A., Richardson, J. D., et al. 2021, ApJL, 915, L26
Galli, A., Baliukin, I. I., Bzowski, M., et al. 2022, SSRv, 218, 31
Galli, A., Baliukin, I. I., Kornbleuth, M., et al. 2023, ApJL, 954, L24
Galli, A., Wurz, P., Fuselier, S. A., et al. 2014, ApJ, 796, 9
Galli, A., Wurz, P., Rahmanifard, F., et al. 2019, ApJ, 871, 52
Galli, A., Wurz, P., Schwadron, N. A., et al. 2017, ApJ, 851, 2
Galli, A., Wurz, P., Schwadron, N. A., et al. 2022, ApJS, 261, 18
Heerikhuisen, J., Zirnstein, E. J., Pogorelov, N. V., Zank, G. P., & Desai, M. 2019, ApJ, 874, 76
Kornbleuth, M., Opher, M., Dialynas, K., et al. 2023, ApJL, 945, L15
Linsky, J. L., & Moebius, E. 2023, ApJ, 942, 45
Livadiotis, G., McComas, D. J., Schwadron, N. A., Funsten, H. O., & Fuselier, S. A. 2013, ApJ, 762, 134
McComas, D. J., Alimaganbetov, M., Beesley, L. J., et al. 2024, ApJS, 270, 17
McComas, D. J., Allegrini, F., Bochsler, P., et al. 2009, Sci, 326, 959
McComas, D. J., Bzowski, M., Dayeh, M. A., et al. 2020, ApJS, 248, 26
McComas, D. J., Christian, E. R., Schwadron, N. A., et al. 2018, SSRv, 214, 116
McComas, D. J., Lewis, W. S., & Schwadron, N. A. 2014, RvGeo, 52, 118
Pogorelov, N. V., Bedford, M. C., Kryukov, I. A., & Zank, G. P. 2016, JPhCS, 767, 012020
Rahmanifard, F., Möbius, E., Schwadron, N. A., et al. 2019, ApJ, 887, 217
Reisenfeld, D. B., Bzowski, M., Funsten, H. O., et al. 2021, ApJS, 254, 40
Richardson, J. D., Burlaga, L. F., Elliott, H., et al. 2022, SSRv, 218, 35
Schwadron, N. A., Allegrini, F., Bzowski, M., et al. 2011, ApJ, 731, 56
Schwadron, N. A., Moebius, E., Fuselier, S. A., et al. 2014, ApJS, 215, 13
Swaczyna, P., Bzowski, M., Dialynas, K., et al. 2024, ApJL, 969, L20
Swaczyna, P., McComas, D. J., Zirnstein, E. J., et al. 2020, ApJ, 903, 48
Zirnstein, E. J., Dayeh, M. A., Heerikhuisen, J., McComas, D. J., & Swaczyna, P. 2021, ApJS, 252, 26
Zirnstein, E. J., Kumar, R., Heerikhuisen, J., McComas, D. J., & Galli, A. 2018a, ApJ, 865, 150
Zirnstein, E. J., Kumar, R., Heerikhuisen, J., McComas, D. J., & Galli, A. 2018b, ApJ, 860, 170